

## Magnetic phase diagram of $\text{Ho}_x\text{Tm}_{1-x}$ alloys

R. S. Sarthour, R. A. Cowley, R. C. C. Ward, and M. R. Wells

*Department of Physics, University of Oxford, Clarendon Laboratory, Parks Road, Oxford, OX1 3PU, United Kingdom*

D. F. McMorrow

*The Condensed Matter Physics and Chemistry Department, Risø National Laboratory, DK-4000 Roskilde, Denmark*

J. Jensen

*Ørsted Laboratory, Niels Bohr Institute, Universitetsparken 5, DK-2100 Copenhagen, Denmark*

(Received 25 February 2000)

The magnetic phase diagram of the competing anisotropy system, Ho/Tm, has been determined by neutron-scattering techniques and the results compared with calculations based on a mean-field model. The crystal-field interactions in Ho favor alignment of the magnetic moments in the basal plane whereas in Tm they favor alignment along the  $c$  axis. Single-crystal alloys were grown with molecular-beam epitaxy techniques in Oxford. The components of the magnetic moment along the  $c$  direction and in the basal plane were determined from the neutron-scattering measurements. Five distinct magnetic phases, with long-range order, were identified and the magnetic phase diagram, including a pentacritical point, determined. A mean-field model was used to explain the results and the results are in good agreement with the experimental results.

### I. INTRODUCTION

The rare-earth metals have many different magnetic structures because of the interplay between the crystal-field and exchange interactions. The situation is even more complex in alloys because the crystal field may favor different directions in each of the alloy constituents. As shown by recent experiments with Ho/Er alloys,<sup>1</sup> there are then many different magnetic phases leading to complex phase diagrams with several multicritical points. There is also one phase that has only short-range order and is completely surrounded by phases with long-range order and could not be understood within the framework of mean-field theory. The experiments reported in this paper are similar experiments for Ho/Tm alloys. They were undertaken so as to establish whether some of the features found in the Ho/Er system were particular to the Ho/Er system or were generic to systems with competing directions for the crystal-field interactions. More explicitly, the crystal field in Ho favors alignment of the magnetic moments in the basal planes perpendicular to the hexagonal  $c$  axis, while for both Er and Tm alignment along the unique  $c$  axis is favored. The difference between Er and Tm is that the crystal field is much stronger in Tm than in Er as shown by the magnetic structures of the bulk metals. For Er the cycloid and cone phases have components of the ordered magnetic moments in both the basal plane and along the  $c$  axis,<sup>2</sup> while for Tm the moments are always aligned along the  $c$  axis.<sup>3</sup>

Bulk Ho orders magnetically below  $T_N \sim 132$  K and its magnetic structure is a basal-plane helix, that transforms to a cone phase on cooling below  $T_C \sim 22$  K.<sup>4</sup> In contrast, bulk Tm has a  $c$  axis longitudinally modulated magnetic structure below  $T_N \sim 58$  K.<sup>3</sup> For both elements, the modulation wave vector is along the  $c$ -axis direction and at low temperatures, the structure is commensurate with a long period due to the crystal-field interactions. In the case of Ho the wave vector is  $\mathbf{q} = \frac{1}{6}\mathbf{c}^*$ , and the magnetic structure has a 12 layer period.

Pairs of the basal plane components of the moments tend to align close to particular  $\mathbf{a}^*$  directions due to the sixth-order crystal-field anisotropy. This structure is represented as (222 222) where the notation means that there are two layers with their magnetic moments aligned close to successive  $\mathbf{a}^*$  axes. At low temperatures, the Tm magnetic structure consists of four moments aligned parallel to the  $c$  axis, followed by three moments aligned in the opposite direction. The structure is then represented as {43} and its wave vector is  $\mathbf{q} = \frac{2}{7}\mathbf{c}^*$ . The numbers inside the brackets { } represent the ordering along the  $c$  axis and the numbers are the number of successive planes aligned in the same direction.

The development of molecular-beam epitaxy (MBE) technique has allowed the growth of materials that are not readily available as single crystals and in the next section, we describe the growth of the alloy films. Neutron-scattering experiments were used to determine the magnetic structures as described in Sec. II. The analysis of the experimental results and the identification of the magnetic structures are described in Sec. III. The predictions of a mean-field model, that was used to help in the identification of the magnetic phases, as well as compared quantitatively with the results, are reported in the Sec. IV. In Sec. V, the theoretical and experimental results are presented and the magnetic phase diagram of the alloys deduced. The results are discussed and conclusions drawn in Sec. VI.

### II. EXPERIMENTAL PROCEDURE

The  $\text{Ho}_x\text{Tm}_{1-x}$  alloy samples were grown by MBE using the Balzers UMS630 facility at Oxford, following the technique described in Ref. 5. A 100-Å buffer layer of Nb was deposited on the epipolished (11 $\bar{2}$ 0) sapphire substrate, in order to prevent chemical reaction between the rare earths and sapphire. A 1000-Å seed layer of nonmagnetic Y was deposited prior to the alloy layer. This epitaxial system leads

to (0001) growth of the hcp rare earths. A series of  $\text{Ho}_x\text{Tm}_{1-x}$  single-crystal alloys was grown by the co-deposition of elemental sources at a substrate temperature of  $\sim 700$  K, with compositions  $x=0, 0.15, 0.30, 0.42, 0.55, 0.65,$  and  $0.75$ . Because both elements have similar melting points and lattice parameters, good single-crystal growth was obtained. The thickness of the alloys was  $10\,000$  Å and they were capped to prevent oxidation of the magnetic alloys with  $150$  Å of Y.

The samples were characterized using a rotating anode x-ray source in Oxford. Scans of the wave-vector transfer along the  $[00l]$  and  $[10l]$  directions in reciprocal space showed that the alloy films are single crystals and have the hcp structure. The mosaic spread at the (002) reflection was between  $0.2$  and  $0.1^\circ$ , for all the samples.

The magnetic structures were determined by elastic neutron diffraction, using the triple axis diffractometer TAS1 at Risø National Laboratory. The samples were oriented so that the  $[h0l]$  plane was the scattering plane. The neutrons were obtained from a cold source, and a monochromatic beam with a wavelength of  $4.05$  Å was selected by a (002) Bragg reflection from a pyrolytic graphite monochromator. In order to suppress contamination by neutrons reflected from higher-order reflections, a Be filter, cooled to  $77$  K, was used. An analyzer—also pyrolytic graphite—reduced the background and improved the instrumental resolution. For the compositions  $x=0.75, 0.55,$  and  $0.3$ , the collimation from reactor to detector was  $\text{open}/30'/60'/141'$  and  $\text{open}/60'/60'/141'$  for the  $x=0.65, 0.42, 0.15,$  and  $0$  concentrations. The intensity of the scattering was corrected for the instrumental resolution using the method described in Cowley and Bates.<sup>6</sup>

Variable-temperature cryostats, transparent for neutrons, were used and the temperature was measured with calibrated platinum and carbon sensors. The temperature was stable to better than  $\pm 1$  K, and the measurements were taken in steps of  $2.5$  K, giving a precision of  $\sim \pm 1.0$  K for the temperatures of the phase transitions.

### III. DATA ANALYSIS

The experiments and their analysis were similar to those performed for the Ho/Er alloys.<sup>1</sup> Scans of the wave-vector transfer  $\mathbf{Q}$  along the  $[00l]$  and  $[10l]$  directions in reciprocal space were performed and the intensities and wave-vector transfers of the (002), (002- $q$ ), (100), and (10 $q$ ) reflections were measured, Fig. 1. The magnetic modulation wave vector  $q$  was determined from the difference between the positions of the nuclear and magnetic reflections, and is given in  $c^*$  units.

For all of the samples, the intensity of the (002) peak did not change with temperature, indicating that the scattering at this position is wholly nuclear in origin. In contrast, temperature-dependent magnetic scattering was observed at the other three positions. The (002- $q$ ) reflection is proportional to the square of the magnetic moments in the basal plane. The (10 $q$ ) reflection is proportional to the square of the magnetic moments in the  $y$  direction of the basal plane and along the  $c$  direction. The magnetic component of the (100) reflection is proportional to a ferromagnetic component along the  $c$  axis. Choosing the  $c$  direction to be parallel to  $z$ ,

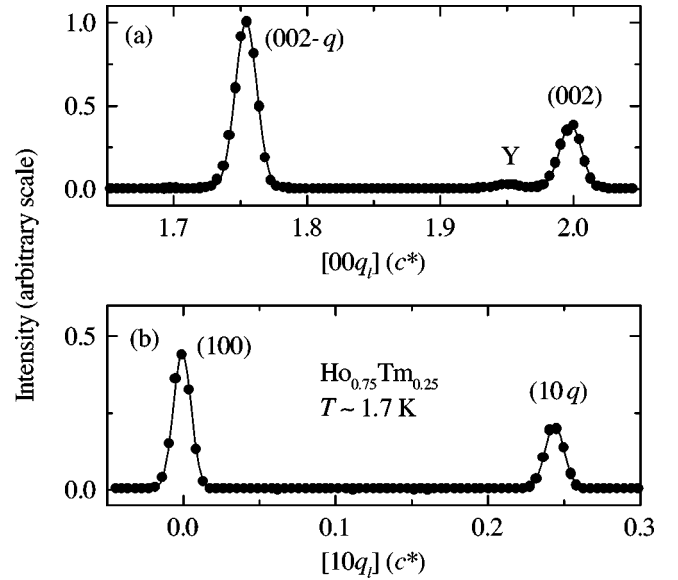


FIG. 1. The scattered intensity for scans of the wave-vector transfer  $q$  along (a) the  $[00l]$  and (b) the  $[10l]$  reciprocal-space directions, at  $T \sim 1.7$  K, for  $\text{Ho}_{0.75}\text{Tm}_{0.25}$ . The integrated intensities and the modulation wave vector  $q$  were determined by fitting the reflections with Gaussians (the lines in the figure). The extra scattering in the plot (a) is due to the Y seed. There is also a magnetic contribution to the (100) reflection, at this temperature.

the contribution of the magnetic scattering to these reflections is given by

$$\begin{aligned} I(002-q) &= F_1[\langle S_x(q) \rangle^2 + \langle S_y(q) \rangle^2], \\ I(10q) &= F_2[0.01\langle S_x(q) \rangle^2 + \langle S_y(q) \rangle^2 + \langle S_z(q) \rangle^2], \\ I_M(100) &= F_3\langle S_z(0) \rangle^2. \end{aligned} \quad (1)$$

The factors  $F_1$ ,  $F_2$ , and  $F_3$  are constants that depend on the instrumental resolution and the magnetic structure factor. The number, 0.01, arises from the polarization factors. The factor  $\langle S_\alpha(q) \rangle$  is proportional to the spatial average of the ordered magnetic moment in the  $\alpha$  direction;

$$\langle S_\alpha(\mathbf{q}) \rangle^2 = \left| \sum_j \langle g_j J_{\alpha j} \rangle \exp(i\mathbf{q} \cdot \mathbf{R}_j) \right|^2. \quad (2)$$

The experimental results were analyzed assuming a random orientation of the magnetic domains, so that  $\langle S_x(q) \rangle^2 = \langle S_y(q) \rangle^2$ . The ratio between  $F_1$  and  $F_2$  was determined by comparing the intensities  $I(002-q)$  and  $I(10q)$  when  $\langle S_z(q) \rangle$  was known to be zero. The (100) and (10 $q$ ) reflections are close in  $\mathbf{Q}$ , so that the magnetic form factor, structure and polarization factors are similar and neglecting these small corrections,  $F_3 = 2F_2$ . The  $\langle S_\alpha(q) \rangle$  values were then extracted from the three magnetic reflections, Eq. (1), and using the appropriate averaged magnetic form factor<sup>7</sup> and the magnetic structure factors, the quantities  $\langle gJ_\perp(q) \rangle$ ,  $\langle gJ_z(q) \rangle$ , and  $\langle gJ_z(0) \rangle$  were determined. The constant  $g$  is the Landé factor and  $\langle gJ_\perp(q) \rangle^2 = \langle gJ_x(q) \rangle^2 + \langle gJ_y(q) \rangle^2$ , which describes the component of the average magnetic mo-

ment in the basal plane. The terms  $\langle gJ_z(q) \rangle$  and  $\langle gJ_z(0) \rangle$  describe the magnetic modulation and the ferromagnetic moment along the  $c$  direction.

The magnetic phases were identified from the components of the magnetic moment as follows:

(i) For a cone phase,  $\langle gJ_\perp(q) \rangle$  and  $\langle gJ_z(0) \rangle \neq 0$ , while  $\langle gJ_z(q) \rangle = 0$ .

(ii) For a basal plane helix,  $\langle gJ_\perp(q) \rangle \neq 0$ , while  $\langle gJ_z(0) \rangle = \langle gJ_z(q) \rangle = 0$ .

(iii) For a  $c$  axis longitudinally modulated,  $\langle gJ_z(q) \rangle \neq 0$ , while  $\langle gJ_z(0) \rangle = \langle gJ_\perp(q) \rangle = 0$ .

(iv) For a tilted helix and a cycloid,  $\langle gJ_\perp(q) \rangle$  and  $\langle gJ_z(q) \rangle \neq 0$ , while  $\langle gJ_z(0) \rangle = 0$ .

It is impossible from our measurements to distinguish unambiguously between a tilted helix and a cycloid phase and hence to identify the transition between them. The tilted helix has different components for the ordered moments along each of the  $x$ ,  $y$ , and  $z$  directions, while the cycloid has components only along  $z$  and a specific direction in the basal plane. However, the intensity observed is an average over all the magnetic domains, and the scattering over a random distribution of magnetic domains for a cycloid is indistinguishable from that of a tilted helix as both have  $\langle gJ_\perp(q) \rangle$  and  $\langle gJ_z(q) \rangle$  nonzero. An average mean-field theory including only the leading crystal-field terms<sup>1</sup> suggests that the transition occurs when

$$R = \langle gJ_\perp(q) \rangle / \langle gJ_z(q) \rangle = 1. \quad (3)$$

However, the theory described in the next section has been used to calculate the value of  $R$  with a more general model for which the transition occurs at larger values of  $R$ , usually between 2 and 3, due to the modifications of the angular variation of the anisotropy energy introduced by the crystal-field terms of higher rank.

#### IV. THEORETICAL MODEL

There are three dominant magnetic interactions in the heavy rare earths: the single ion anisotropy due to the crystal field, the Heisenberg exchange coupling, and the classical magnetic dipole-dipole interaction. The Hamiltonian is written<sup>8</sup>

$$\begin{aligned} \mathcal{H}_0 = & \sum_i \sum_{lm} B_l^m O_l^m(i) - \frac{1}{2} \sum_{ij} \mathcal{J}(ij) \mathbf{J}_i \cdot \mathbf{J}_j \\ & - \frac{1}{2} \sum_{ij} \mathcal{J}_D(ij) J_{ci} J_{cj}. \end{aligned} \quad (4)$$

The  $\mathcal{J}(ij)$  are the exchange constants and  $B_l^m, O_l^m$  are the crystal-field parameters and the Stevens operators, respectively, while the  $\mathcal{J}_D(ij)$  arise from the dipole-dipole interaction. The Fourier transform of the coupling is  $\mathcal{J}(q)$ , and

TABLE I. The crystal-field parameters used in the mean-field calculations in units of meV.

$B_l^m$	$B_2^0$	$B_4^0$	$B_6^0$	$B_6^6$
Ho	0.024	0.0	$-9.56 \times 10^{-7}$	$9.21 \times 10^{-6}$
Tm	-0.096	0.0	$-9.2 \times 10^{-6}$	$8.86 \times 10^{-5}$

since the modulation in this system is always along the  $c$  direction it can be written in terms of the interplanar constants  $\mathcal{J}_n$ , as may be seen from Eq. (4):

$$\mathcal{J}(q) = \mathcal{J}_0 + 2 \sum_n \mathcal{J}_n \cos(nqc/2). \quad (5)$$

The isotropic part of the dipole-dipole interaction is included in the effective exchange interaction leaving only the  $cc$  component in the third term. The classical contribution vanishes at  $q=0$ , and for nonzero  $q$  it may be written as

$$\mathcal{J}_D(q) = -\mathcal{J}_{dd} [0.919 + 0.0816 \cos(qc/2) - 0.0006 \cos(qc)] \quad (6)$$

The coupling constant  $\mathcal{J}_{dd}$  is 0.0349 and 0.0305 meV, for Tm and Ho, respectively.<sup>9,12</sup> The only crystal-field terms allowed for the hcp structure have  $l=2, 4, 6$  and  $m=0$  and  $l=m=6$ . The Heisenberg exchange and the dipolar coupling are both two-ion interactions. For the calculations, both terms were simplified using the mean-field approximation (MFA),<sup>8</sup> in which the fluctuations of the moments are neglected, and the Heisenberg exchange term for the ion at the  $i$ th site is given by

$$\mathcal{H}_{\text{ex}}(i) = \left( \mathbf{J}_i - \frac{1}{2} \langle \mathbf{J}_i \rangle \right) \cdot \sum \mathcal{J}(ij) \langle \mathbf{J}_j \rangle. \quad (7)$$

The term under the summation is the mean field at the  $i$ th site, and  $\frac{1}{2} \langle \mathbf{J}_i \rangle$  is a correction to avoid double counting. The magnetic structure is found by an iterative numerical procedure, which consists of choosing an initial distribution of moments  $\langle \mathbf{J}_j \rangle$ , and diagonalizing the MF Hamiltonian for each site. The partition function and free energy are calculated as well as new set of  $\langle \mathbf{J}_j \rangle$  and the process repeated until self-consistency is achieved.

The crystal-field parameters and the coupling parameters used in the present calculations are given in Tables I and II, respectively. The parameters for Tm are those obtained by McEwen *et al.*<sup>9</sup> In the case of Ho,<sup>12</sup> the temperature dependence of the exchange parameters is simplified by using the parameters in Table II for most of the phase diagram. The trigonal coupling, which only contributes with a very small term to the free energy, is neglected. In the alloy system  $\text{Ho}_x\text{Tm}_{1-x}$ , the magnetic structures are calculated using the virtual crystal approximation, and the exchange coupling

TABLE II. The interplanar exchange coupling coefficients given in units of meV.

$\mathcal{J}_n$	$\mathcal{J}_0$	$\mathcal{J}_1$	$\mathcal{J}_2$	$\mathcal{J}_3$	$\mathcal{J}_4$	$\mathcal{J}_5$	$\mathcal{J}_6$
Ho	0.263	0.100	0.010	-0.029	-0.005	0.008	-0.004
Tm	0.098	0.057	-0.022	-0.025	-0.010	-0.002	0.0

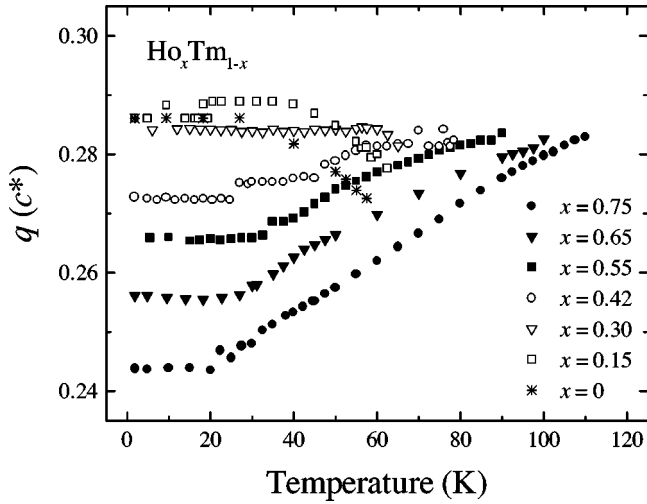


FIG. 2. The wave vector  $q$ , given in units of  $c^*$ . The error bars were omitted, but the accuracy in the wave vectors is  $\pm 0.002c^*$ .

constants between the different kinds of ions are constructed from a linear interpolation between the constants in pure Ho,  $\mathcal{J}_{\text{Ho}}(ij)$ , and pure Tm,  $\mathcal{J}_{\text{Tm}}(ij)$ , scaled with the appropriate factors

$$\mathcal{J}_{A-B}(ij) = (g_A - 1)(g_B - 1) \left( x \frac{\mathcal{J}_{\text{Ho}}(ij)}{(g_{\text{Ho}} - 1)^2} + (1 - x) \frac{\mathcal{J}_{\text{Tm}}(ij)}{(g_{\text{Tm}} - 1)^2} \right), \quad (8)$$

where each of the indices  $A$  or  $B$  denotes either a Ho or a Tm ion.

## V. MAGNETIC STRUCTURES

Single-crystal thin films of  $\text{Ho}_x\text{Tm}_{1-x}$ , with the nominal compositions  $x = 0.75, 0.65, 0.55, 0.42, 0.30, 0.15$ , and  $0$ , were studied and the different magnetic phases identified. The transition temperatures are labeled as in<sup>1</sup>  $T_{RS}$  where  $R$  and  $S$  specify the two phases with  $P, H, T, C, L, \text{Co}$  corresponding to the paramagnetic, basal-plane helix, tilted helix, cycloid, longitudinally modulated, and cone phases, respectively.

The temperature dependence of the modulation wave vector  $q$  is shown in Fig. 2. It was obtained from the wave vectors of the  $(002-q)$  and  $(10q)$  reflections, and no significant differences were observed between the two observations, except for the sample with  $x = 0.42$ , as discussed below. At low temperatures, the wave vector locks into a commensurate value and then on warming  $q$  increases for the  $x \geq 0.42$ , while for  $x = 0.3$ ,  $q$  is independent of temperature, and for  $x < 0.3$   $q$  decreases.

### A. ( $x = 0.75$ )

The temperature dependence of the magnetic moments,  $\langle gJ_{\perp}(q) \rangle$ ,  $\langle gJ_z(q) \rangle$ , and  $\langle gJ_z(0) \rangle$ , is presented in Fig. 3. At the lowest temperature,  $\langle gJ_z(0) \rangle$  and  $\langle gJ_{\perp}(q) \rangle$  are nonzero and the structure is a cone with an angle of  $\sim 26^\circ$ . On heating to  $T_{\text{TCo}} = 20$  K,  $\langle gJ_z(q) \rangle$  becomes nonzero, while  $\langle gJ_z(0) \rangle$  is negligible because of a first-order transition from the cone

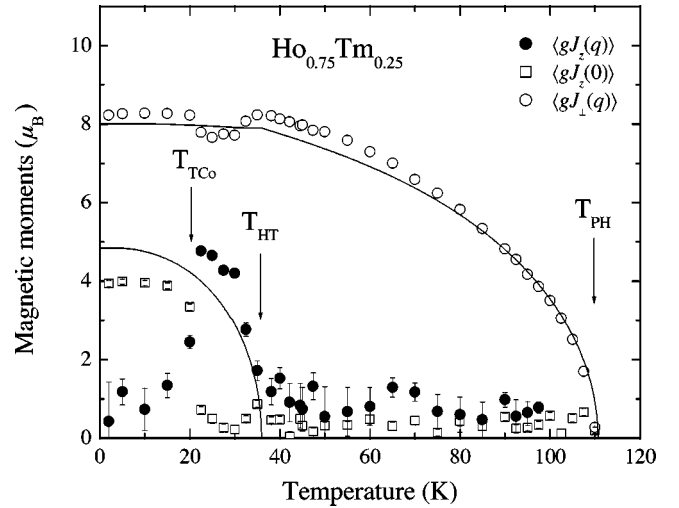


FIG. 3. The ordered magnetic moments for  $\text{Ho}_{0.75}\text{Tm}_{0.25}$ . The open circles are the basal plane moment, the solid circles the modulated  $c$ -axis moment and the open squares the ferromagnetic  $c$ -axis moment. The solid lines are the results of the model.

to a tilted helix phase. Above a higher temperature  $T_{\text{HT}} = 35$  K,  $\langle gJ_z(q) \rangle$  is negligible, and there is a transition from a tilted helix to a basal plane helix. The transition to a paramagnetic phase occurs at  $T_{\text{PH}} = 110$  K. The wave vector  $q = 0.244c^*$ , below 20 K, in the cone phase and this corresponds to the basal plane spin-slip structure  $[221(211)]^9$ . Above 20 K, the wave vector increases smoothly with increasing temperature. The results from the mean-field model correctly predict the observed phases and the values of  $T_{\text{HT}}$  and  $T_{\text{PH}}$ , but a slight modification in the anisotropy parameters is necessary to give the transition temperature  $T_{\text{TCO}}$ , to the cone phase.

### B. ( $x = 0.65$ )

The sample with the concentration  $x = 0.65$ , has only two magnetically ordered phases. Between  $T_{\text{PH}} = 99$  K and  $T_{\text{HT}} = 45$  K, the structure is a basal-plane helix and below  $T_{\text{HT}}$  it is a tilted helix. The model gives a good description of these phases. At low temperatures the wave vector  $q = 0.256c^*$  is close to the commensurate value  $\frac{10}{39}$ , and corresponds to the  $[(211)^2 2111]$  spin-slip structure.

### C. ( $x = 0.55$ )

The measured  $\langle gJ_{\perp}(q) \rangle$  and  $\langle gJ_z(q) \rangle$  and the results of the mean-field calculation are shown in Fig. 4. Between  $T_{\text{HT}} = 50$  K and  $T_{\text{PH}} = 91$  K, the structure is a basal plane helix. The model accounts for the magnetization curves in the helical and tilted helical phases, but suggests (the dashed line) a first-order transition to the cycloid at about 11 K. No evidence for this transition was found in the experiment.

### D. ( $x = 0.42$ )

The sample is magnetically ordered below  $T_{\text{PH}} = 80$  K, and  $\langle gJ_{\perp}(q) \rangle$  is nonzero, Fig. 5, so the magnetic structure is a basal plane helix. As the temperature decreases below  $T_{\text{HT}} = 57.5$  K  $\langle gJ_z(q) \rangle$  becomes nonzero and the structure becomes a tilted helix. The mean-field calculations are in

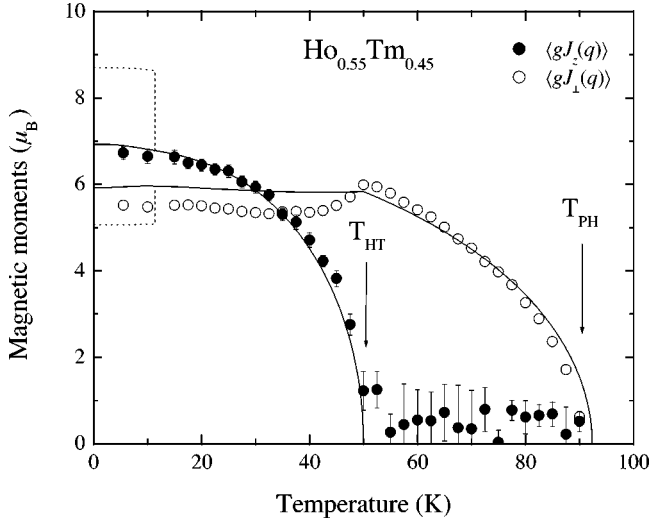


FIG. 4. The ordered magnetic moments for  $\text{Ho}_{0.55}\text{Tm}_{0.45}$ . The open circles are the basal plane moment and the solid circles the modulated  $c$ -axis moment. The solid lines are the results of the model.

agreement with both  $T_{HT}$  and  $T_{PH}$  and give the transition from a tilted helix to a cycloid at 45 K when  $R$  [see Eq. (3)] is about 2. The model predicts a kink at the transition and a more rapid increase of  $\langle gJ_z(q) \rangle$  in the cycloidal than in the tilted phase. Experimentally, the ordered  $c$ -axis moment behaves more like that obtained by the model when the transition to the cycloidal phase is suppressed (the dashed line obtained by a slightly modified model) indicating that the most likely possibility is that the structure stays in the tilted phase at all temperatures below  $T_{HT}$ .

Unexpectedly, the results show that the basal plane and  $c$  axis components have different modulation wave vectors at certain temperatures, Fig. 6. At low temperatures below 25

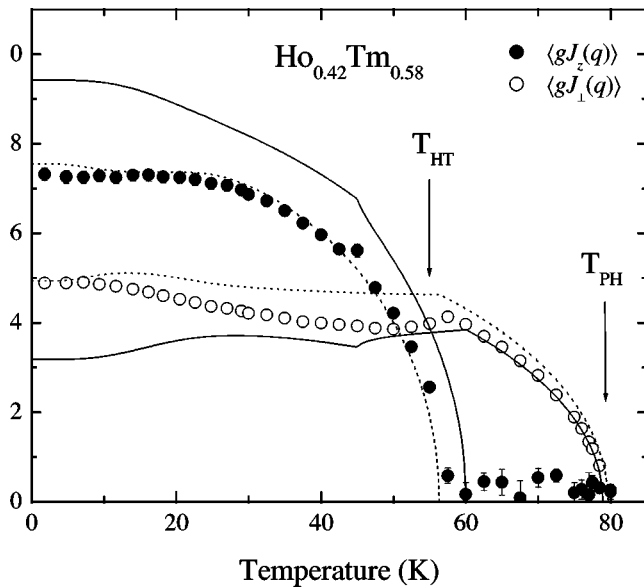


FIG. 5. The ordered magnetic moments for  $\text{Ho}_{0.42}\text{Tm}_{0.58}$ . The open circles are the basal plane moment and the solid circles the modulated  $c$ -axis moment. The solid lines are the results of the model and the dotted lines of the model when modified to suppress the cycloid.

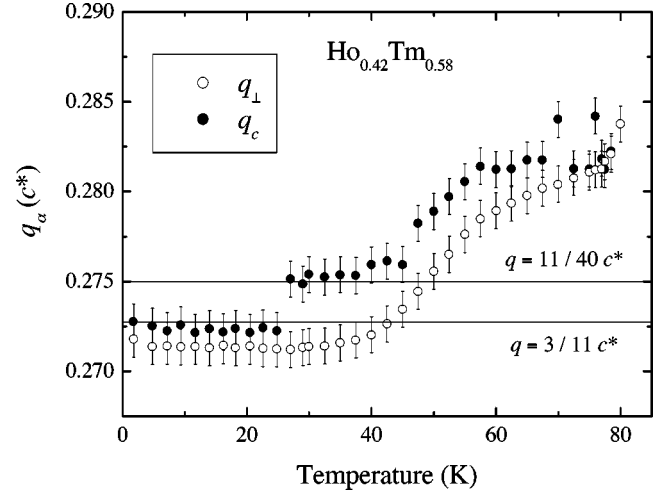


FIG. 6. The temperature dependence of the wave vectors for the basal plane and modulated  $c$ -axis components— $q_{\perp}$  and  $q_z$ —given in  $c^*$  units, for the  $x=0.42$  concentration.

K, both have the same wave vector, within the experimental uncertainties ( $q_{\perp} = q_z = 3/11c^*$ ), which corresponds to the commensurate spin-slip  $(211\ 121\ 111)$  structure. However, at  $T \sim 25$  K,  $q_z$  increases abruptly to  $11/40c^*$ , that corresponds to a  $\{43(443)^3\}$  lock-in structure for the  $c$ -axis components. Above  $T=45$  K, both wave vectors increase but  $q_z$  is consistently the larger except possibly above 60 K.

#### E. ( $x=0.30$ )

Two magnetic phases occur for the concentration  $x = 0.30$ , in agreement with the mean-field model as illustrated in the Fig. 7. Above  $T_{LC} = 57.5$  K, the structure is longitudinally modulated while below  $T_{LC}$ , it is a cycloid. The onset of magnetic order occurs at  $T_{PL} = 66$  K, and the mean-field model predicts correctly the transition temperature. The wave vector  $q = 0.284c^*$  is close to  $q = 2/7c^*$ , and independent of temperature.

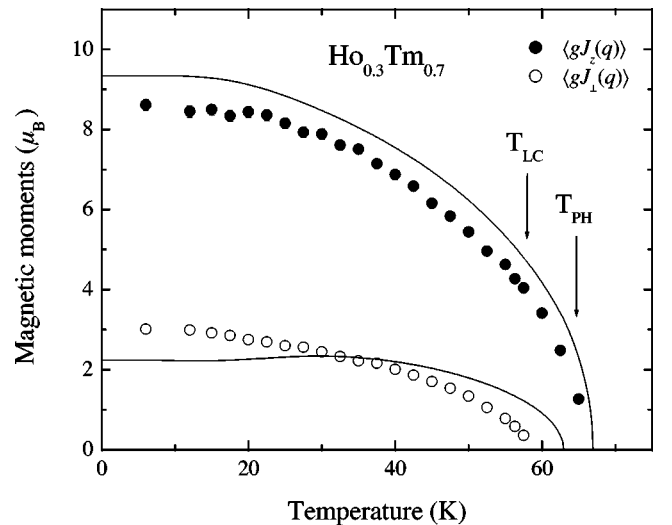


FIG. 7. The ordered magnetic moments for  $\text{Ho}_{0.30}\text{Tm}_{0.70}$ . The open circles are the basal plane moment and the solid circles the modulated  $c$ -axis moment. The solid lines are the results of the model.

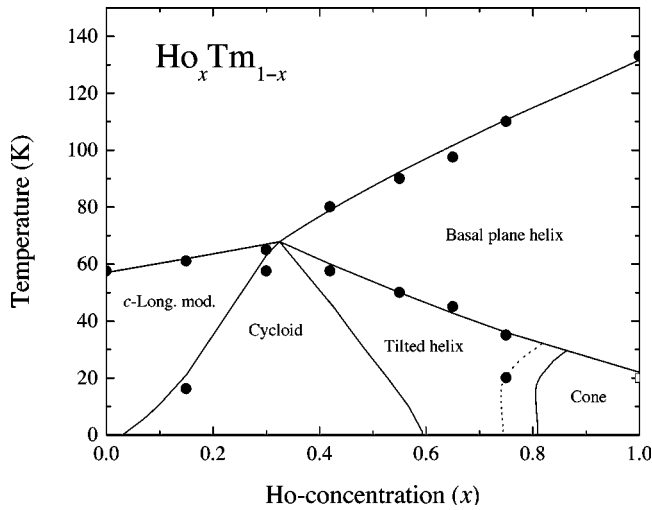


FIG. 8. The magnetic phase diagram of the  $\text{Ho}_x\text{Tm}_{1-x}$  alloys. The closed circles show the transition temperatures observed and the lines are the model predictions. The dashed line shows the result calculated with a small modification of the original model to account for the cone phase. The open square indicates the transition temperature to a cone phase as observed in bulk Ho, but not in the pure film and the open circles show the transition to the phase with  $q_{\perp}$  different from  $q_z$ .

#### F. ( $x=0.15$ )

The results for the alloy with the concentration  $x=0.15$  are similar to those for  $x=0.30$ . There are two magnetic phases and  $T_{LC}=16.7$  K and  $T_{PL}=61.5$  K. The mean-field model predicts correctly both transition temperatures. At low temperatures, the wave vector  $q=(2/7)c^*$  and corresponds to the  $\{43\}$   $c$ -axis spin-slip structure of bulk Tm and on heating above 40 K,  $q$  decreases.

#### G. ( $x=0$ )

The pure Tm film gave results similar to those of bulk Tm.<sup>2</sup> The magnetic structure is longitudinally modulated below the Néel temperature,  $T_{PL}=61.5$  K, and is correctly predicted by the mean-field model. The commensurate value of the wave vector  $q=\frac{2}{7}c^*$ , below 30 K, corresponds to the  $\{43\}$  structure, and above 30 K  $q$  decreases. However, the moment obtained for  $\langle gJ_z(q) \rangle$  was slightly higher at low temperature, than that observed in the bulk or calculated by the model. We are uncertain whether this is due to experimental error, or a thin-film effect.

## VI. DISCUSSION

Figure 8 illustrates the magnetic phase diagram for the  $\text{Ho}_x\text{Tm}_{1-x}$ . The lines are the calculated phase boundaries and the points are the transition temperatures obtained from the experiment. The points for  $x=1$  correspond to the transition temperatures of bulk Ho, but the cone phase is suppressed in the thin films of Ho similar to those of our alloys.<sup>5,10</sup> As may be seen from the phase diagram, the mean-field model predicts correctly the values of  $T_{HT}$  and  $T_{PH}$ , for all compositions, and the existence of the penta-critical point at  $x_c=0.325$  and  $T_c=67.85$  K. For  $x=0.75$ , a slight modification of the anisotropy terms in the model is

necessary to account for the first-order transition from the tilted helix to the cone phase (the modified result is shown by the dashed line on the figure). The model also accurately predicts the transition temperatures from a cycloid to a longitudinally modulated phase ( $T_{LC}$ ) and then to the paramagnetic phase ( $T_{PL}$ ). The change of a cycloid to a tilted helix cannot be observed directly so there is more uncertainty about the determination of this phase boundary. This is also valid for the theoretical model, as the position of this phase line depends sensitively on the values of the fourth and sixth rank axial anisotropy parameters, which are also the most uncertain ones. However, the indications are that the phase line between the cycloid and the tilted phase is steeper than shown in Fig. 8, as the phase transition does not occur at  $x=0.55$  and probably also not at  $x=0.42$ .

For the alloy with  $x=0.42$ , the wave vector of the basal plane component  $q_{\perp}$  is different from that of the  $c$  component  $q_z$ . The mean-field model was modified to allow for the differences in the wave vectors. The free energy of these structures was then compared with those obtained when  $q_{\perp}=q_z$ . There were only very small differences, and the amplitudes of the first harmonics of the moments are nearly equal. A possible reason that the lock-in effect between  $q_{\perp}$  and  $q_z$  is weak, may be seen from the relative contributions of the Tm and the Ho ions to the different components (at about 5 K):

$$\langle J_{\perp}(q_{\perp})/J \rangle_{\text{Ho}}=0.85, \quad \langle J_z(q_z)/J \rangle_{\text{Ho}}=0.66;$$

$$\langle J_{\perp}(q_{\perp})/J \rangle_{\text{Tm}}=0.14, \quad \langle J_z(q_z)/J \rangle_{\text{Tm}}=1.26.$$

For the Tm ions the basal plane components are small and the  $c$ -axis component is large, whereas the situation is almost the opposite for the Ho ions. This means that the coupling of the modulations of the  $c$  component and of the basal plane components is smaller in this mixed system than in a more uniform one. The structure may therefore be able to take advantage of a different wave vector for the maximum in  $\mathcal{J}(q)$  for the basal plane and the  $c$  component, by choosing two different ordering wave-vectors. Furthermore, this decoupling also favors a helical ordering of the basal plane components in comparison with the linear one (i.e., the cycloid) implying that a type of tilted helix phase is more likely to occur than a cycloid.

The wave vector  $q$  increases with increasing temperature for phases with an ordered moment in the basal plane, whereas it decreases for those phases with the longitudinally modulated structure. This effect is also observed for Ho/Er (Ref. 1) alloys and for bulk Er.<sup>2</sup> The temperature dependence of the wave vector for a helix was explained by Elliot and Wedgwood.<sup>11</sup> The magnetic ordering splits the energy bands of the conduction electrons at the Fermi level, and that the total energy is a minimum if the wave vector decreases as the ordered moment increases.

The change of the wave vector from that at the onset of the magnetic ordering,  $\Delta q=q_{PH}-q$ , where  $q_{PH}$  is the value of  $q$  at  $T_{PH}$ , is shown in Fig. 9 as a function of the basal plane ordered moment. The results are described by the power law

$$\Delta q=xC\langle gJ \rangle^n, \quad (9)$$

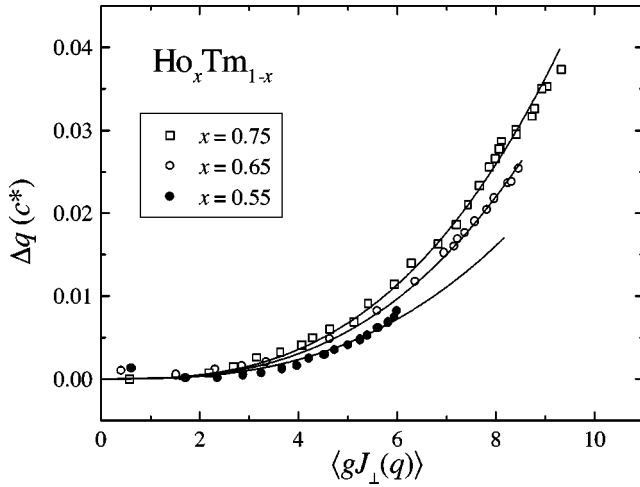


FIG. 9. The change of the ordering wave vector ( $\Delta q = q_N - q$ ) as a function of the basal plane moment for the  $x=0.75$ ,  $0.65$ , and  $0.55$  concentrations.

where  $C$  is a constant,  $x$  the Ho concentration and  $\langle gJ \rangle$  the measured basal plane moment. The lines in the Fig. 9 are fits to Eq. (6), with  $n = 2.6 \pm 0.2$  and  $C = 1.8 \pm 0.5 \times 10^{-5}$ . This behavior and the value of the exponent are consistent with those found for Ho/Er alloys.<sup>1</sup>

The average electron-gas model used for determining the  $x$  dependence of the effective exchange constants, Eq. (7), predicts correctly the concentration dependence of the phase line between the paramagnetic and the antiferromagnetic phases, on both sides of the pentacritical point. However, the variation of the ordering wave vector with  $x$  indicates a more complex behavior of the exchange interaction. One compli-

cation is the anisotropy indicated by the occurrence of different ordering wave vectors for the  $c$  and the basal plane components in the  $x=0.42$  alloy. The same kind of anisotropy is detected in the  $x$  dependence the ordering wave vector  $q$ . The model predicts a roughly linear variation, but the observations are that the wave vector stays nearly constant,  $q \approx 0.283$ , at the transition between the paramagnet and the helix, i.e., for  $x$  larger  $x_c$ , and changes linearly from  $0.273$  to  $0.283$  at the transition involving the ordering of the  $c$ -axis moments, when  $x$  is changed from  $0$  to  $x_c$ .

## VII. CONCLUSIONS

The magnetic phase diagram of the  $\text{Ho}_x\text{Tm}_{1-x}$  alloys has been determined using neutron diffraction. The results are compared with the predictions of a mean-field model of the alloys. As may be seen from the phase diagram, Fig. 8, the theoretical model is in good agreement with the experiment, predicting the transition temperatures and the values of magnetic moments,  $\langle gJ_z(q) \rangle$  and  $\langle gJ_\perp(q) \rangle$ , within the experimental and theoretical uncertainties, for most of the concentrations of the alloys. The results show that the phase diagram has a pentacritical point and near this concentration, the modulation wave vector of the basal plane and longitudinally moments differed.

## ACKNOWLEDGMENTS

Financial assistance from the EPSRC in the UK, CAPES in Brazil, and the LIP program of the EU is gratefully acknowledged.

<sup>1</sup>R. A. Cowley, J. A. Simpson, C. Bryn-Jacobsen, R. C. C. Ward, M. R. Wells, and D. F. McMorrow, *Phys. Rev. B* **57**, 8394 (1998).  
<sup>2</sup>R. A. Cowley and J. Jensen, *J. Phys.: Condens. Matter* **4**, 9673 (1992).  
<sup>3</sup>W. C. Koehler, J. W. Cable, E. O. Wollan, and M. K. Wilkinson, *Phys. Rev.* **126**, 1672 (1962).  
<sup>4</sup>W. C. Koehler, J. W. Cable, M. K. Wilkinson, and E. O. Wollan, *Phys. Rev.* **151**, 414 (1966).  
<sup>5</sup>D. A. Jehan, D. F. McMorrow, R. A. Cowley, R. C. C. Ward, M. R. Wells, and N. Hagmann, *Phys. Rev. B* **48**, 5594 (1993).  
<sup>6</sup>R. A. Cowley and S. Bates, *J. Phys. C* **21**, 4113 (1988).

<sup>7</sup>J. Brown, *International Tables for Crystallography* (Dordrecht, 1983) Vol. C.  
<sup>8</sup>J. Jensen and A. R. Mackintosh, *Rare Earth Magnetism* (Oxford University Press, Oxford, 1991).  
<sup>9</sup>K. A. McEwen, U. Steigenberger, and J. Jensen, *Phys. Rev. B* **43**, 3298 (1991).  
<sup>10</sup>J. A. Borchers, M. B. Salamon, R. W. Erwin, J. J. Rhyne, R. R. Du, and C. P. Flynn, *Phys. Rev. B* **43**, 3123 (1991).  
<sup>11</sup>R. J. Elliot and F. A. Wedgwood, *Proc. Phys. Soc. London* **81**, 846 (1963).  
<sup>12</sup>J. Jensen, *Phys. Rev. B* **54**, 4021 (1996).